

Graphene oxide additive-driven widening of microporous biochar for promoting water pollutant capturing

Yaoheng Liang^{a,1}, Xuejun Xu^{a,1}, Fangzheng Yuan^{a,1}, Yinlei Lin^a, Yisheng Xu^a, Yuyuan Zhang^a, Dongchu Chen^a, Wenyi Wang^c, Huawen Hu^{a,**}, Jian Zhen Ou^{b,*}

^a School of Materials Science and Hydrogen Energy, Foshan University, Foshan, 528000, China

^b School of Engineering, RMIT University, Melbourne, Victoria, 3000, Australia

^c Department of Applied Biology and Chemical Technology, The Hong Kong Polytechnic University, Hung Hom, Kowloon, 999077, Hong Kong, China

ARTICLE INFO

Keywords:

Microporous biochar
Micropore widening
Hierarchical porosity
Carbon-based composites
Environmental remediation

ABSTRACT

Renewable and low-cost biochar's intrinsic porous structure limitations make its porous structure mediation highly significant for performance enhancement. We employ graphene oxide (GO) as an additive at a low dosage for the deed-leaf-derived biochar's microporous structure mediation to promote the wastewater treatment ability toward a typical antibiotic pollutant - tetracycline hydrochloride (TCH). While KOH-based activation enables biochars with a microporous structure and improved graphitization, GO transforms part of micropores of such activated biochar into mesopores (i.e. forming hierarchical porosity), driven by the thermal pyrolysis of oxygen groups enriched on GO. The GO additive-induced process overcomes the loss of surface resulted from conventional pore widening, promoting mass transport as well as improving the accessibility to pore interiors and compatibility for large-size contaminant molecules. The increase of the sp^2 -to- sp^3 carbon ratio from 0.59 to 0.79 with GO incorporation facilitates π - π stacking interactions with aromatic pollutants (including TCH and organic dyes), which are more critical than the electrostatic attraction and hydrogen bonding interactions. Apart from superior adsorption capacities of 193.43 and 336.70 mg/g obtained at 303 and 313 K, respectively, the graphene-modified hierarchically porous biochar is recyclable, reusable, resistant to interfering metal cations, and universal for binding a range of organic pollutants bearing different charge states, demonstrating equilibrium adsorption capacities of 186.58, 190.38, 268.43, and 254.88 mg/g for TCH, methylene blue, Rhodamine B, and methyl orange, raised by 26.8%, 41.6%, 32.1%, and 105.3%, respectively, compared to the counterpart without GO-enabled micropore widening. The greater adaptability to different-size pollutants presents higher practical application viability.

1. Introduction

The fast development of various industries also poisons the living cycles of humans, especially the aquatic environment and related biosphere [1]. Antibiotics are one industrial product category that can severely contaminate the water environment because of their infectious and recalcitrant nature, thus posing a growing threat to living organisms [2]. Considering the panic COVID-19 epidemic worldwide, the management of antibiotics has become the focus of widespread attention since they might be the epidemic source or induce the mutation of the virus [3]. Therefore, there is a pressing need for the development of

functional materials to deal with antibiotics efficiently [4].

Functional materials-based purification of antibiotics has been widely reported, such as photocatalysis [5], Fenton's reagent-based advanced oxidation [6], chemical reduction [7], biodegradation [8], chemical flocculation [9], adsorption [10], and a combination thereof [11]. Among them, adsorption is the most economical and suitable for on-site treatments since no other chemicals are required except an adsorbent [12]. More importantly, antibiotic purification based on adsorption can be free from secondary pollution that is usually accompanied by other purification processes (e.g., while photocatalysis likely generates toxic intermediates, biodegradation produces large amounts

* Corresponding author.

** Corresponding author.

E-mail addresses: huawenhu@126.com (H. Hu), Jianzhen.ou@rmit.edu.au (J.Z. Ou).

¹ These authors contributed equally to this work.

of sludge) [13,14].

Numerous adsorbents have been reported to capture antibiotics, especially biochar- and graphene-based materials [13,15]. Along with the exploration of different kinds of graphene-based materials (especially the adsorbents constructed by graphene oxide (GO) [16] and reduced graphene oxide (rGO) [17]), various biochar is fabricated using diverse natural resources (e.g., corncob [18], orange peels [19], banana peels [20], pomelo peels [21], bagasse [22], dead leaves [23], municipal sludge [24], etc. [25]). While graphene materials possess a unique two-dimensional (2D) planar structure, giant specific surface area, and remarkable adsorption ability, the biochar is featured in large specific surface areas, rich porosity, and abundant oxygen/nitrogen (O/N)-containing functional groups [26–29]. The rational engagement of graphene with biochar is expected to combine both merits to produce high-performance carbon-based adsorbents for environmental remediation. Nevertheless, the unresolved high-cost issues of graphene materials make them inappropriate for use as the main matrix, and their dosage should be minimized. On the contrary, renewable and cheap biochar promises to be used as the substrate for adsorbent construction. Therefore, employing graphene as an additive to modify the biochar-based substrate is reasonable and desirable [13].

Although activated biochar possesses a large specific surface and abundant microporosity, making it promising for practical adsorption purification of antibiotics-contaminated water, its micropore-dominated internal structure limits the adsorption performance and, meanwhile, constrains the mass transport within the microporous structure. The micropore widening treatments of different biochar materials have been demonstrated to be favorable for enhancing the adsorption performances (e.g., micropore widening that was achieved by tuning the high-temperature carbonization atmosphere [30] and by dry mixing activation treatment [31]). Nevertheless, the research outcome focusing on biochar micropore widening for enhanced environmental remediation performance is rarely reported, possibly due to the grand challenge of tailoring the microporous structure of biochar-based materials in a controlled manner given that satisfactory pore widening cannot be achieved under either weak or strong processing conditions. For example, too strong activation processing may collapse porous structure and mainly form the macroporous structure, which is unfavorable for achieving high adsorption capacity.

In this context, we present the first example to engineer the intrinsic microporous structure of the activated biochar derived from dead leaves using GO additive at a low loading content. While the pristine activated biochar is dominated by microporous architecture, GO transforms part of the micropores of the biochar substrate into mesopores, giving rise to hierarchical porosity. Although GO additive is applied at a low dosage, its 2D structure and enriched oxygen groups can strongly perturb the internal structure of biochar during the carbonization of the biomass-activation agent mixture. Such GO additive-induced micropore-to-mesopore transformation is demonstrated to increase the accessibility of the internal adsorption sites, improve mass transport and, consequently, promote the adsorption of tetracycline hydrochloride (TCH). This typical antibiotic has been undergoing intense current attention worldwide. Besides, the graphene composition can strengthen the interactions with TCH through π - π stacking interactions. The structure and adsorption performance of the biochar-based adsorbents before and after graphene additive incorporation are systematically characterized and analyzed, while the adsorption kinetics, isotherms, and thermodynamics are investigated at the same time. The generality of the biochar-based adsorbents for treating organic pollutants bearing different charge states, as well as recyclability, reusability, and the anti-interfering ability against typical metal cations that commonly exist in tap water, are assessed. More importantly, the mechanisms underlying pollutant adsorption over the biochar-based materials bearing different porous structures are presented.

2. Experimental

2.1. Raw materials

The dead leaves of the Banyan tree were collected from our campus. The analytical reagents, TCH, KOH, and NaOH, were purchased from the Shanghai Macklin Biochemical Co., Ltd (Shanghai, China). Rhodamine B (RhB), an analytical reagent, was provided by the Tianjin Damao Chemical Reagent Factory (Tianjin, China). The methyl orange (MO) and methylene blue (MB) dyes (analytical purity) were obtained from the Tianjin Guangfu Fine Chemical Engineering Institute (Tianjin, China) and Tianjin Tianxin Fine Chemical Development Center (Tianjin, China), respectively. The analytical reagents (sodium chloride (NaCl) and anhydrous calcium chloride (CaCl₂)) were purchased from the Tianjin Yongda Chemical Reagent Co., Ltd. (Tianjin, China) and Guangzhou Jinhua Chemical Reagents Co., Ltd (Guangdong, China). All of the other chemicals adopted in the present study were analytical reagents and used without further purification unless stated otherwise.

2.2. Preparation of microporous and hierarchically porous biochar-based adsorbents

The dead leaves of the Banyan tree were cleaned with deionized (DI) water many times until the DI water became clear. After drying the cleaned dead leaves in a vacuum oven at 100 °C for 8 h, they were sufficiently pulverized using a high-speed pulverizer and then passed through a 100-mesh sieve to produce a uniform biomass powder. Afterward, the dead leaf powder (10.0 g) was mixed with KOH powder (10.0 g) and GO (0.5 g). After thoroughly ground for homogenization, the mixture was subject to a calcination treatment in a tubular furnace. The grinding treatment in the presence of KOH could homogeneously disperse GO within the dead-leaf biomass matrix through the formation of potassium salts for facile mixing (Fig. S1 in the Supplementary Data (SD)) and the grinding force-enabled homogenization (Fig. S2 in the SD). Then, pyrolysis was carried out under the following conditions: the temperature was raised to 700 °C at a rate of 10 °C/min, which was then maintained for 2 h. The high-temperature pyrolysis could also help exfoliate graphene and form a homogenous dispersion within the biochar matrix (Fig. S2 in the SD). After cooling to room temperature, the powder was withdrawn and thoroughly washed with diluted hydrochloric acid (5.0 wt%). It was further cleaned with DI water until the filtrate became clear, with a pH of 7. The washed powder was dried under vacuum at 60 °C for 2 h, yielding the hierarchically porous biochar-based sample designated as KBCG. For comparison, activated biochar bearing primary microporosity was also prepared according to the above procedures, except that GO was not involved. The activated biochar of microporosity was designated as KBC. Besides, the biochar (termed BC) was fabricated without KOH activation or GO incorporation and used as another control. The schematic illustration of the preparation of the BC, KBC, and KBCG samples is presented in Fig. 1, which also depicts their representative structural features, especially porosity variation among these samples.

2.3. Adsorption experiment

Batch adsorption experiments were adopted to assess the adsorption performance of the prepared BC, KBC, and KBCG samples. The impact of different parameters (e.g., pH, initial TCH concentrations, temperature, contact time, and presence of metal cations) on the adsorption performance of these samples toward TCH were investigated (see experimental details in the SD). The recycling and reusing performance of the KBCG sample was also evaluated by six cycles of adsorption and desorption of TCH. Furthermore, the generality of the samples was proved by capturing different kinds of adsorbates in addition to TCH, including MB, RhB, and MO. In addition to the above adsorption experiments, more are provided in the SD in detail, including the

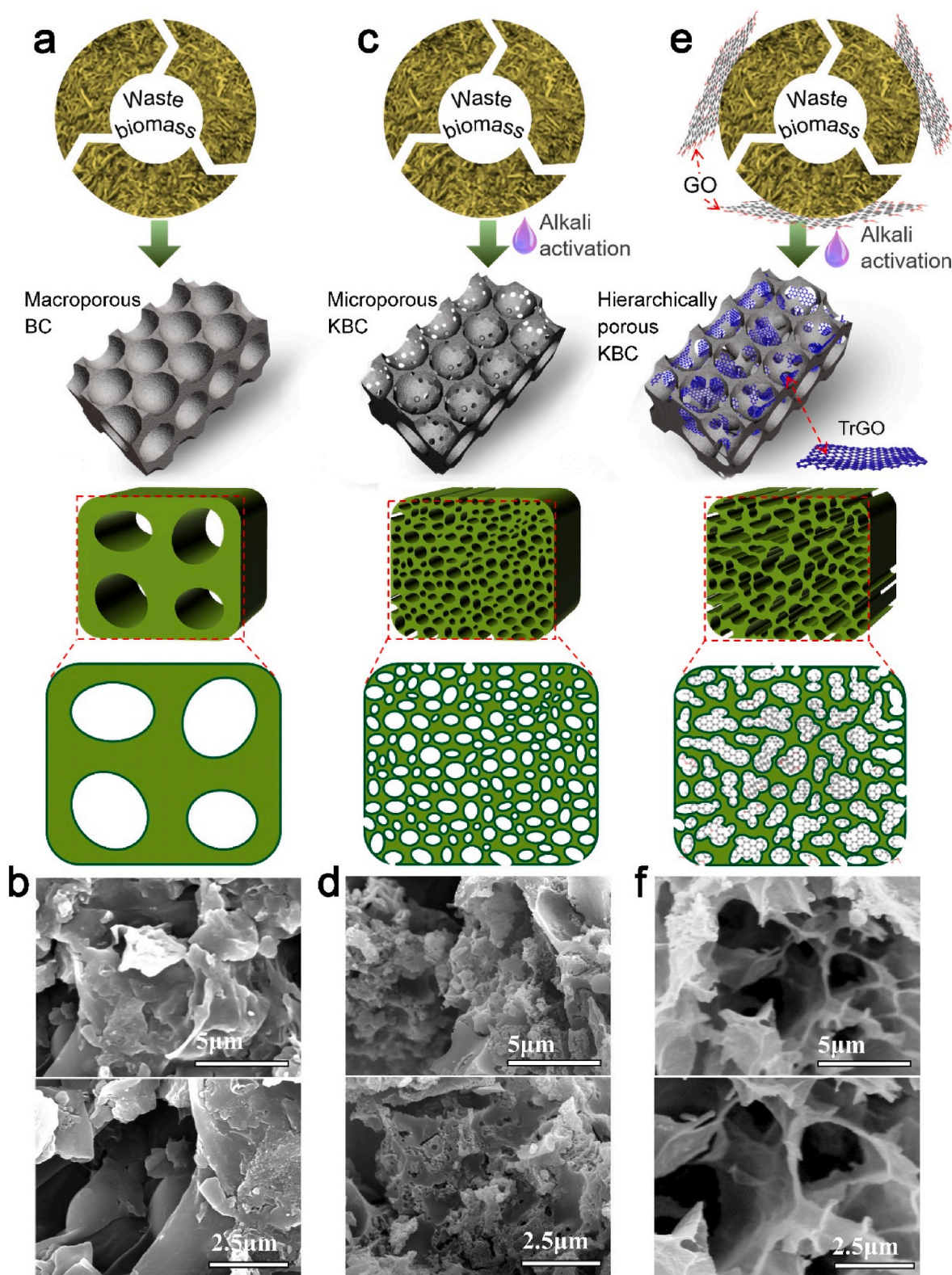


Fig. 1. Regulating the porous structure of biochar-based adsorbents derived from the Banyan tree dead leaves by alkali activation and GO-induced micropore widening. (a–f) Schemes (a, c, and e) and SEM images at different magnification scales (b, d, and f) presenting the pore structure evolution from macroporous BC (a and b), microporous KBC (c and d), to hierarchically porous KBCG (e and f).

isothermal adsorption process and adsorption kinetics.

For the adsorption tests, the contaminant concentration was determined according to Beer-Lambert's Law based on the UV-Vis absorbance at $\lambda = 357$ nm for the TCH contaminant. The real-time adsorption

amount at time t (q_t , mg/g) and the equilibrium adsorption amount (q_e , mg/g) were determined based on Equations 1 and 2, respectively:

$$q_t = \frac{(C_0 - C_t) \times V}{m} \quad (1)$$

$$q_e = \frac{(C_0 - C_e) \times V}{m} \quad (2)$$

where C_0 (mg/L) is the initial concentration before the adsorption treatment, C_t (mg/L) is the TCH concentration when the adsorption proceeded for time t (min), V (mL) is the volume of the aqueous solution containing TCH, and m (g) is the dosage of the biochar-based adsorbent.

3. Results and discussion

3.1. Structural and morphology analysis of biochar-based adsorbents

The structural evolution from BC, KBC to KBCG is revealed by schemes and SEM images at different magnification scales (Fig. 1a–f). Pure dead-leaf biomass powder exhibits a sheet-like structure while lacking interconnected pores (Fig. S3 in the SD), indicating that it is necessary to engineer the pure biomass structure to impart graphitization, enrich porosity, and boost adsorption performance. After carbonization in the absence of KOH, some pores are developed for the BC sample, albeit with fewer interconnected pores (Fig. 1b). The carbonization of dead-leaf biomass in the presence of KOH results in a much different morphology of KBC from that of BC, and an enriched microporous structure can be observed for KBC (Fig. 1d). The generation of numerous micropores can be due to the corrosive KOH that etches the carbon substrate to generate gas bubbles and develop the microporous structure (Equation (3) ~ 7) [32–34].



Nevertheless, the micropores might be too small to accommodate the contaminant molecules, which is unfavorable for synthesizing high-performance biochar-based adsorbents. Thus, the microporous structure of activated biochar is further tuned with GO additive. The resulting KBCG exhibits a hierarchical porosity (Fig. 1e and f), in stark contrast to the microporous KBC prepared without involving the GO additive. Thus, this finding reveals that the GO additive plays a critical role in widening the microporous biochar. We assume that the enriched oxygen groups of GO layers are pyrolyzed to generate an adequate impact on the internal structure of the activated biochar substrate, thus merging part of micropores into mesopores while leaving a certain number of micropores due to the limited addition amount of the GO additive. As a result, the hierarchical porosity of the KBCG sample is obtained, as exhibited by SEM images.

3.2. BET-specific-surface area and pore analysis

To further elucidate the role of KOH and the GO additive in engineering the porous structure of the biochar-based adsorbent, we turned to the N_2 adsorption-desorption measurements. The results are

Table 1
Summary of the results obtained via the N_2 adsorption-desorption test.

Sample	BET-specific-surface area (m^2/g)	Total pore volume (cm^3/g)	Average pore size (nm)
Pure biomass	19.1	0.020	4.2
BC	41.8	0.049	4.7
KBC	510.5	0.385	3.0
KBCG	394.1	0.322	3.3

presented in Fig. S4 (SD) and Table 1. Indeed, a lack of porous structure of pure biomass provides a limited specific surface area and total pore volume. Although the straightforward carbonation of dead leaves without KOH (resulting in the BC sample) can somewhat increase the specific surface area and total pore volume relative to the pure biomass precursor, the increments are not evident. The BC's type-II N_2 physisorption isotherm reveals a non-porous or primarily microporous nature (see the scheme shown in Fig. 1). By KOH activation, the KBC biochar can be produced with a markedly increased specific surface area ($510.5 \text{ m}^2/\text{g}$) and total pore volume ($0.385 \text{ cm}^3/\text{g}$) as compared with the BC counterpart prepared without KOH activation, thus revealing the critical role of KOH activation in forming highly porous biochar. Notably, a small hysteresis loop appears for KBC, attributed to the capillary condensation from mesopores, and the type-IV isotherm can thus be assigned. Nevertheless, the inconspicuous hysteresis loop and a steep rise at low relative pressures indicate that KBC primarily possesses micropores (i.e., KBC is microporous).

Interestingly, incorporating a small amount of GO as an additive for biochar's porous structure mediation can enlarge the hysteresis loop based on the type-IV isotherm for the KBCG sample, thus revealing that more mesopores are generated due to GO-induced micropore widening compared with the KBC counterpart. This micropore widening is of great significance in promoting pollutant enrichment via improving the accessibility of the pore interiors, promoting mass transfer, and raising the compatibility between the size of the pollutant and the porous structure. The hysteresis loop type of H4 can be noted for KBCG, indicating the highly porous substrate of the activated biochar. Although the micropore widening decreases the specific surface area of KBCG compared with KBC (510.5 vs. $394.1 \text{ m}^2/\text{g}$). Since a micropore size probably matches that of N_2 molecules during the N_2 physisorption test, the numerous micropores of KBC contribute to the impressive specific surface area. The larger size of TCH relative to N_2 might make it incapable of diffusing into KBC micropores. The inaccessible micropores indicate the waste of adsorption sites buried thereof. Therefore, the micropore widening into mesopores is necessary to increase the accessible adsorption sites. The engineering of the microporous structure with the GO additive can increase the average pore size of KBCG compared with that of the KBC sample prepared without involving the GO additive (3.3 vs. 3.0 nm). From the hysteresis loops shown in Fig. S4 (SD), the more explicit loop can be observed for the KBCG sample at a high relative pressure range, indicating the strengthened mesoporous nature favorable for contaminant adsorption. Even though the GO additive-induced micropore widening causes a loss of specific surface area, it is still at a high level ($394.1 \text{ m}^2/\text{g}$) compared to a wide range of reported porous biochars and their composites with graphene and others [35–42], as summarized in Table S1 (SD). Significantly, the micropore widening can bring many benefits for pollutant capturing (e.g., enhanced mass transport, improved adsorption site accessibility, and increased accommodation capacity for pollutants of large sizes). A promoted mass transfer can also be revealed by a lower powder density of KBCG than those of other samples, as exhibited by a larger volume at the same sample weight (Fig. S5 in the SD).

3.3. Structural and composition analysis by TEM and elemental mapping

Consistent with the results obtained via SEM, the structure of pure biomass powder is also sheet-like under TEM (Fig. 2a and b), and no crystalline fringes can be noted for the pure biomass particle in a high-resolution TEM image presented in Fig. 2c. After carbonization to yield the BC sample, crystalline fringes appear with the distance of the interplanar crystal spacing estimated to be 0.38 nm (Fig. 2d and f), greater than the theoretical value of (002) interplanar spacing of graphite, that is, 0.34 nm . This result might indicate that the straightforward carbonization process without KOH activation cannot produce a highly crystalline graphitic structure. The presence of KOH enables better carbonization, as evidenced by the (002) interplanar crystal

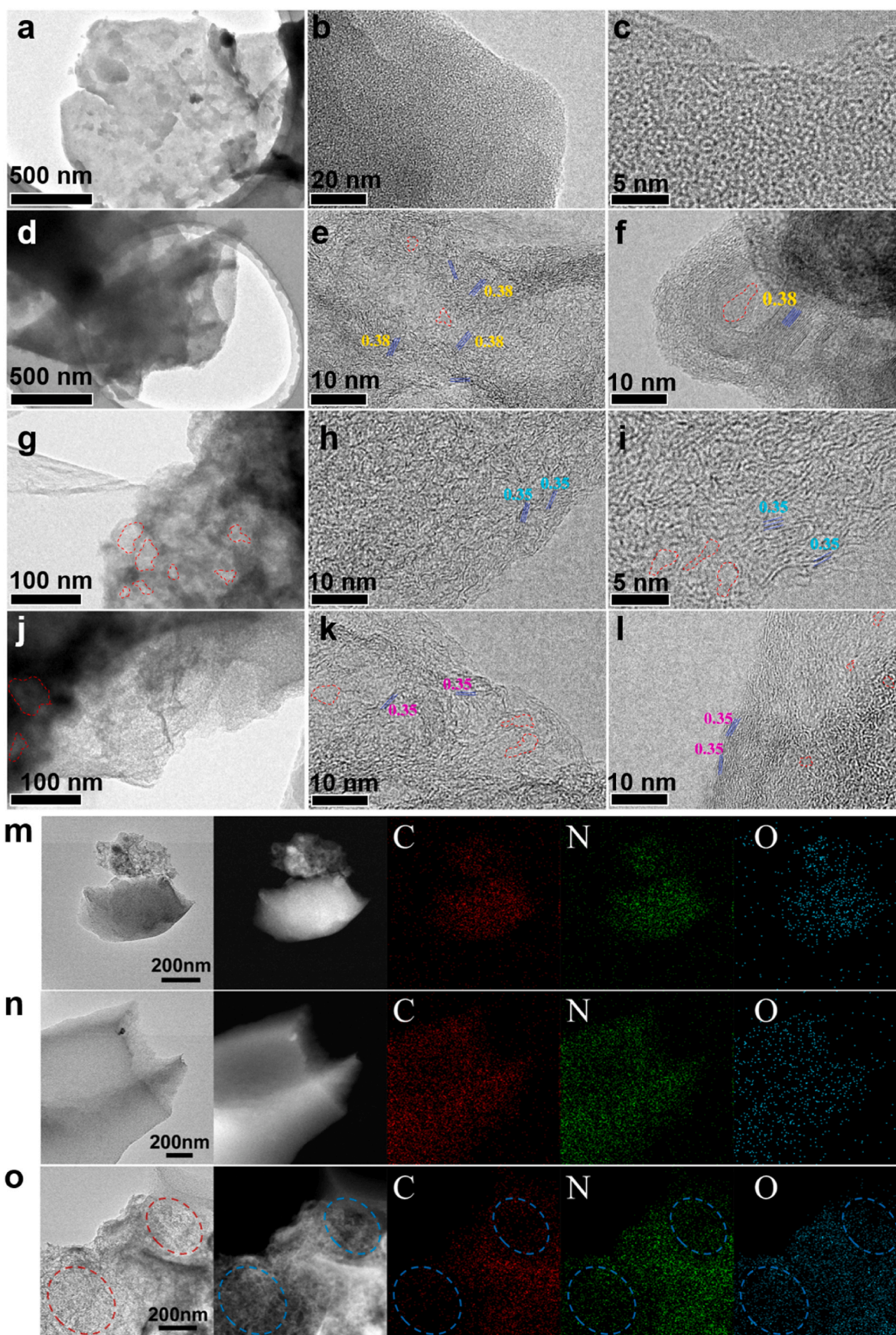


Fig. 2. Structural and composition variations among biomass and different biochar-based samples. (a–l) TEM images of the pure biomass powder (a–c), BC (d–f), KBC (f–i), and KBCG (j–l). (m–o) Elemental mapping images of the BC (m), KBC (n), and KBCG (o) samples.

spacing observed for the KBC sample, closer to that of ideal graphite than the BC counterpart prepared in the absence of KOH (Fig. 2g and i). Therefore, KOH can not only notably increase the specific surface area of biochar but help graphitize the carbon-based structure. The presence of KOH makes the carbon-based substrate more exposed to heat during carbonization, thus better thermally restoring the graphitic carbon structure. This explanation also suits the KBCG sample that presents the (002) carbon interplanar spacing of 0.35 nm (Fig. 2j and l). Besides the crystalline fringes that can be observed, some pores can also be noted for these biochar-based samples, especially for KBC and KBCG. These pores are formed due to the intertwined biochar-based sheet structure. The interconnection between biochar and thermally reduced graphene oxide (TrGO) sheets can also result in stacked pores.

Along with TEM observation, elemental mapping images are also captured for the typical BC, KBC, and KBCG samples, and the results are shown in Fig. 2m, n, and o, respectively. All of these samples show three compositional elements (i.e., carbon, nitrogen, and oxygen), thus indicating the presence of plentiful O/N-containing functional groups. Their presence is conducive to capturing contaminant molecules via H bonding, electrostatic attraction, and cation- π interactions. Interestingly, it can be observed that the KBCG sample exhibits highly porous

domains that are mainly composed of O and N. As highlighted by dashed oval circles, the presence of the C element is faint, in contrast to that of the striking O and N elements. Thus, the porous structure is likely formed by the KOH-enabled etching of carbon substrate (Equation (3) ~ 7). The porous structure can be more hydrophilic than the carbon-rich planar structure of KBCG due to the hydrophilic O/N-containing functional groups. The O/N-containing groups on the internal surface of the porous structure might be favorable for binding the organic contaminants bearing polar functional groups.

3.4. Analysis of crystalline phases, structural defects, and surface properties

XRD patterns of the pure biomass, BC, KBC, and KBCG samples are presented in Fig. 3a. Pure biomass powder exhibits several sharp peaks over a broad bump at approximately 21° due to the presence of some minerals within the pure biomass that had not been washed with acids. For the BC sample prepared by carbonization and acid washing treatments, the broad peak shifts to a larger angle value (around 23.1°) enabled by high-temperature graphitization. Besides, the sharp peaks observed for pure biomass power almost disappear entirely, revealing

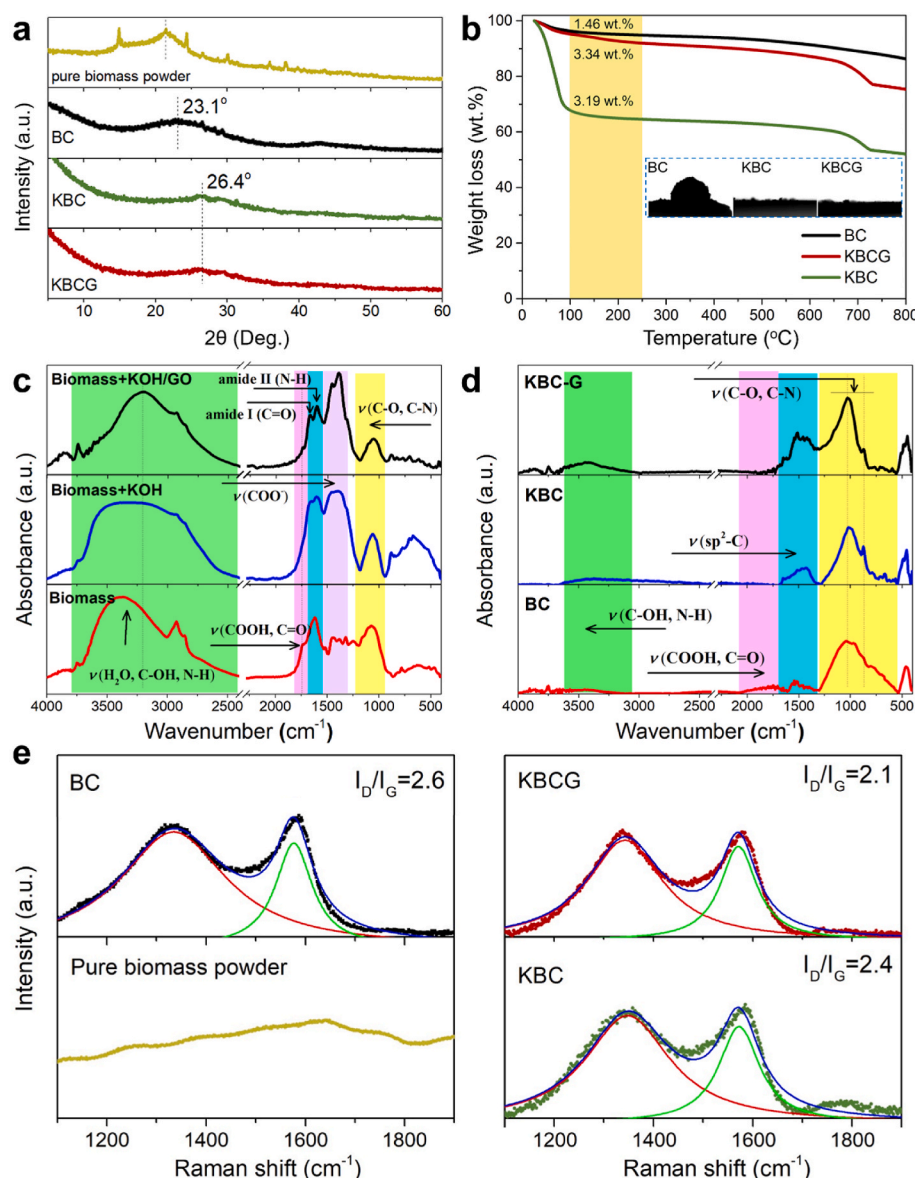


Fig. 3. Probing the variations of crystalline phases, surface properties, and structural defects among different samples. (a-e) XRD patterns (a), TG curves (b), FTIR spectra (c,d), and Raman spectra (e) of various samples. Note that the specimens shown in (c) are the precursors for producing different biochar-based samples based on thermal carbonization. Inset in (b) is the WCA test results for different biochar-based samples (i.e., BC, KBC, and KBCG) that had been compressed on a glass slide before the WCA test.

that the carbonization and acid-washing processes produce a high-purity biochar sample. A further redshift of the angle values can be noted for the KOH-activated biochar samples (including KBC and KBCG), reaching approximately 26.4° , close to the theoretical value of ideal graphite. These results indicate that the KOH-assisted carbonization can improve the graphitization of biochar and lead to activated biochar samples bearing more graphite microcrystallites, consistent with the TEM observation shown in Fig. 2. We also note that KBC and KBCG show a steeper increase in the XRD line intensity over a low-angle range below 10° compared with BC, indicating their improved porosities that the N_2 physisorption study has earlier demonstrated.

The TG curves, shown in Fig. 3b, reveal that the KBC sample possesses a much higher water affinity, as evidenced by the sharp weight loss in the temperature range below 100°C . Compared with BC, the enhanced hydrophilicity of KBC can be due to the KOH-enabled etching of hydrophobic carbon from the biochar substrate and incorporation of hydrophilic functional groups, as well as the generation of porous structure that can impart a capillary condensation effect on water adsorption. The impaired hydrophilicity observed for KBCG relative to that for KBC can be attributed to the incorporation of hydrophobic TrGO sheets. Given that the liable functional groups can be pyrolyzed over the temperature range of $100\text{--}250^\circ\text{C}$ [43], their relative weight percentage can be estimated. KOH can etch part of carbon from the biochar substrate (Equation (3) ~ 7), bringing oxygen groups that account for larger weight percentages than those without involving KOH. The speculation can be verified by an increase in the liable functional group content for KBC and KBCG relative to BC. The transformation of the hydrophobic surface of BC to hydrophilic ones of KBC and KBCG can also be well proven by the water contact angle (WCA) measurements (inset of Fig. 3b).

In contrast to a significant WCA on the compressed BC powder, the water droplets can penetrate the compressed KBC and KBCG powder, indicating improved hydrophilicity. The enhanced hydrophilicity of KBC and KBCG can also be reflected by UV–Vis tests, as shown in Fig. S6 (SD). BC shows much lower UV–Vis absorption across the whole wavelength range when compared with KBC and KBCG, resulting from the more hydrophobic surface of BC that cause heavier aggregations in water media. KBC can be better dispersed in water than KBCG because KBCG contains a more hydrophobic TrGO moiety embedded within the hydrophilic activated biochar substrate. The UV–Vis absorption bands noted for the BC, KBC, and KBCG samples below 230 nm can be indexed to $\pi \rightarrow \pi^*$ electron transition from $\text{C}=\text{C}$ bonds, thus verifying the high-temperature carbonization results in the generation of the π -conjugated carbon structure. The incorporation of graphene composition enables this UV–Vis absorption band to be red-shifted, likely due to the enhancement of the π -conjugated structure. The presence of TrGO, capable of conducting heat [44], during the high-temperature carbonization process helps better graphitize the biochar matrix. Besides, the KOH-based activation also brings the oxygen groups for KBC and KBCG samples, as evidenced by the UV–Vis absorption near 300 nm stemming from $n \rightarrow \pi^*$ electron transitions.

FTIR spectra are further adopted to analyze the thermally induced structural conversion of the dead-leaf biomass and their mixtures with KOH and KOH/GO, and identify the surface functional groups of the corresponding BC, KBC, and KBCG samples. The FTIR spectra of the precursors before carbonization and the carbonized counterparts are provided in Fig. 3c and d, respectively. The pure dead-leaf biomass precursor exhibits much more distinct absorption peaks (Fig. 3c), especially those at approximately 3200 and 1750 cm^{-1} , attributable to the $-\text{OH}-\text{NH}$, $-\text{C}=\text{O}$, and $-\text{COOH}$ groups. The peak observed at around 1618 cm^{-1} is also distinct, which can be assigned to the adsorbed water molecules and amide II (i.e., $\text{N}-\text{H}$ group) of the dead-leaf matrix. Mixing KOH with the pure biomass powder allows the $-\text{COOH}$ groups to be deprotonated into the ionized $-\text{COO}^-$ counterpart. The same results can be obtained for the precursor consisting of dead-leaf biomass, KOH, and GO. We also note that the presence of GO lowers the FTIR absorption

indexed to the amide groups of the precursor comprising the pure biomass, KOH, and GO, compared with the counterpart consisting of biomass and KOH. This finding might be due to the hydrogen bonding interactions between the amide groups of the biomass and the oxygen groups of GO. Such interactions between the biomass matrix and GO can facilitate the subsequent GO-induced biochar micropore widening during the thermal carbonization process.

The high-temperature thermal carbonizations of these precursors, including biomass, biomass + KOH, and biomass + KOH/GO, lead to the generation of different biochar samples corresponding to BC, KBC, and KBCG, respectively. The thermal carbonization significantly weakens the FTIR absorption bands, particularly for $-\text{OH}$ groups, due to the enhanced hydrophobicity and removal of hydrophilic groups imparted via thermal carbonization (Fig. 3d). The pyrolysis-enabled graphitization of biochar samples can be evidenced by the absorption peak around 1500 cm^{-1} stemming from the stretching vibrations of the sp^2 -conjugated carbon network. Notably, KBC exhibits a stronger FTIR absorption around 1500 cm^{-1} compared with BC due to the better graphitization in the presence of KOH that helps create abundant micropores and expedite the heat transfer, which is in good consistence with the results obtained via XRD characterizations (Fig. 3a). The GO additive mediation can further intensify this FTIR absorption band due to the formation of more sp^2 -hybridized carbons.

Raman spectra of various samples are presented in Fig. 3e. While D and G bands reflect the sp^3 -hybridized carbon defects and sp^2 -hybridized graphitic carbon, respectively, the Raman D band-to-G band intensity (I_D/I_G) ratios can elucidate the structural defects and disorders existing in different samples. Before carbonization, pure biomass powder shows no distinct D and G bands of carbon, revealing that the high-temperature calcination plays a critical role in transforming the mixture of organics in the pure biomass into carbon microcrystallites. For the BC sample prepared by direct carbonization of the pure biomass, two distinct Raman peaks can be noted at approximately 1335 and 1580 cm^{-1} . With the assistance of KOH, the KBC biochar can be formed with a higher degree of carbonization compared with the BC counterpart prepared without KOH activation, as verified by a decrease in I_D/I_G . The presence of both KOH and GO yields the KBCG sample with the lowest I_D/I_G value of 2.1 compared with that of BC and KBC. These results reveal that the presence of KOH can help graphitize the biochar and reduce structural defects because KOH contributes to the increased surface area and pore volume, enabling the heat to be more easily transferred for carbonization. The GO additive drives the widening of part of the micropores of the biochar substrate to mesopores with elevated accessibility (see the results obtained via N_2 physisorption measurements shown in Table 1 and Fig. S4 in the SD), and the resulting hierarchical porosity of KBCG is more favorable for heat transfer over the biochar matrix. Besides, the graphene component is reported to be an excellent thermal conductor [44] and capable of promoting the deoxygenation of the biochar matrix [41], facilitating carbonization and graphitization. These results are in good agreement with those obtained via XRD.

XPS is further adopted to unravel the surface composition and chemical states of elements of different samples. The BC, KBC, and KBCG samples are primarily comprised of C, N, and O, thus revealing that the present fabrication and cleaning processes can remove the other elemental impurities from these samples. High-resolution XPS $\text{C}1s$, $\text{O}1s$, and $\text{N}1s$ spectra are then provided to clarify the surface structures, as shown in Fig. 4 and Table S2 (SD). The original biomass consists of $\text{C}=\text{C}/\text{C}-\text{C}$, $\text{C}-\text{O}/\text{C}-\text{N}$, and $\text{C}=\text{O}$, observed at approximately 284.8 , 286.4 , and 287.8 eV , respectively (Fig. 4a) [45]. While retaining the $\text{C}-\text{O}/\text{C}-\text{N}$ groups, the high-temperature carbonization can transform the $\text{C}=\text{O}$ groups into carboxyl groups noted at 289 eV (Fig. 4a), which might imply that the ester groups contained in the pure biomass can be converted to the carboxyl groups with high thermal stability. While C and N percentages are slightly decreased, O content increases from $13.13\text{ at.}\%$ for pure biomass powder to $15.08\text{ at.}\%$ for the BC sample (Table S2 in

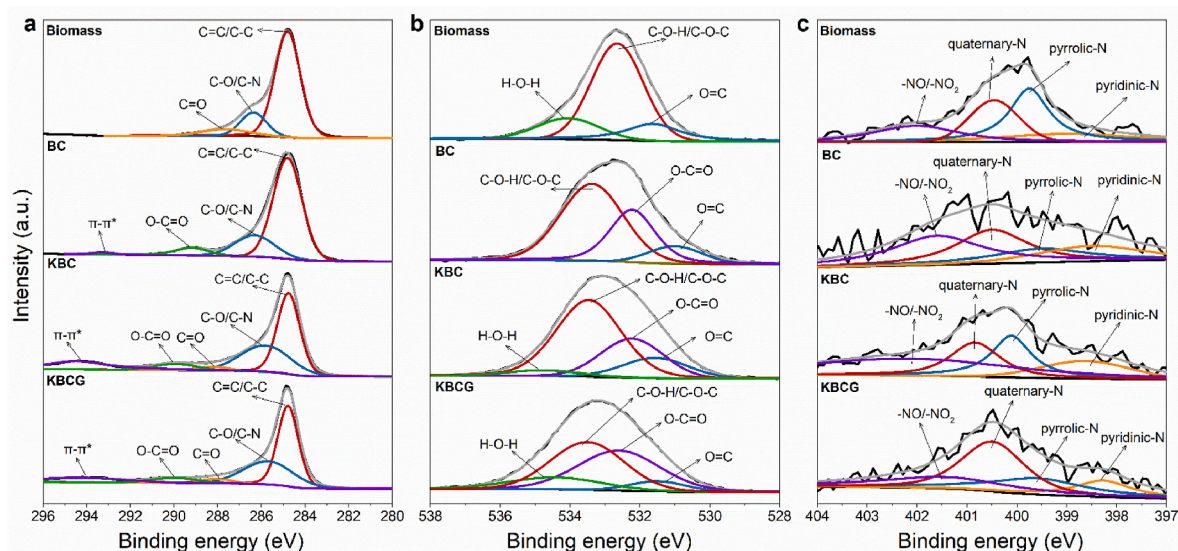


Fig. 4. Chemical state and composition analysis by XPS spectroscopy. (a–c) High-resolution XPS C1s (a), O1s (b), and N1s (c) spectra of the pure biomass, BC, KBC, and KBCG samples.

the SD). Many small organic molecules in the pure biomass are thermally liable to degrade completely. Consequently, elemental compositions are varied in an irregular pattern.

Nevertheless, the thermal pyrolysis in N_2 highly graphitizes the biomass, and a new π - π^* satellite peak at higher binding energies begins to emerge, originating from the vibrations of the aromatic rings of the biochar-based substrate [46]. The KOH activation increases the intensity of such an interesting peak for KBC and KBCG (see the satellite peak marked for KBC and KBCG in Fig. 4a), likely due to the promotion effect of KOH on graphitization. Compared with BC, ester groups ($C=O$) appear for KBC and KBCG, thus implying that KOH can also help incorporate more oxygen-containing groups of different types into the biochar matrix, consistent with the results summarized in Table S2 (SD). The sp^2 -to- sp^3 carbon ratios are also estimated as 0.59 and 0.79 for KBC and KBCG, respectively (Fig. S7 in the SD), revealing that the GO additive can also improve the π -conjugated structure that is favorable for capturing aromatic pollutants via π - π stacking interactions.

The high-resolution XPS O1s spectra show the associated water in the pure biomass sample, corresponding to the peak around 534 eV (Fig. 4b) [47]. The direct carbonization of the pure biomass to yield BC makes the peak corresponding to water disappear, thus indicating that the carbonization process can remove most smaller molecules, such as water and organics. Nevertheless, KOH activation allows the resulting KBC and KBCG samples to be enriched with O/N-containing functional groups (particularly O), thus enhancing hydrophilicity and affinity to water molecules. Four types of N configurations can be deconvoluted from the high-resolution XPS N1s spectra: pyridinic, pyrrolic, quaternary (or graphitic), and oxidized nitrogen, which can be noted at approximately 398.5, 399.5, 400.5, 401.6 eV, respectively [48]. Compared with KBC, the binding energies of the peaks relating to different N configurations are right-shifted for KBCG, probably indicating the intermolecular interactions between the TrGO and N-containing groups (Fig. 4c). Given that the nitrogen content is markedly lower than oxygen (Table S2 of the SD), the role of the nitrogen-containing functional groups should be less critical than oxygen groups. The KOH activation is significant in improving the porosity and incorporating oxygen groups into the biochar matrix, which is favorable for contaminant capturing via the promotion of mass transfer and creation of binding sites, as well as increasing the probability of accommodation of large-size contaminant molecules.

3.5. Adsorption performance analysis

BC exhibits an adsorption performance much inferior to KBC and KBCG over the entire pH range examined (Fig. 5a), thus implying that the KOH activation is essential to improve the microporous structure, specific surface area, surface functionalities and, consequently, adsorption performance of the biochar. Notably, the GO additive can enhance the adsorption performance of KBCG over the entire pH range compared to that of KBC. Considering that KBCG possesses a lower content of oxygen groups and a smaller specific surface area than KBC, the GO-enabled micropore widening plays a pivotal role in the adsorption performance enhancement, which improves the accessibility of the pore interiors and promotes mass transport. Meanwhile, we measured the Zeta potentials of the prepared BC, KBC, and KBCG samples (Fig. 5b). Only in the highly acidic water media do the BC, KBC, and KBCG samples exhibit the positive charge, with the $pH_{pzc} = 2$ –3. On the other hand, as an amphoteric molecule bearing polyionized functional groups, TCH was mainly in the form of TCH_3^+ at the pH values of ≤ 3.3 , which turned out to be the TCH_2^0 form at pH values ranging from 3.3 to 7.7 [49,50]. When the pH value was increased to over 7.7, TCH was changed to be in the anionic form (TCH^- or TC^{2-}). These results explain the lower adsorption capacity achieved at lower pH values due to the electrostatic repulsion interactions between TCH_3^+ and the biochar-based adsorbents. With the rise of the pH, the biochar surface becomes negatively charged, and the electrostatic repulsion is depressed. Because BC possesses fewer O/N-containing functional groups, it is less influenced by the pH. While the optimized pHs for KBC and KBCG can be noted as 4–6, where electrostatic repulsion and π - π stacking interactions are limited and strengthened, respectively. Since KBC has more oxygen groups but inferior adsorption performance compared with KBCG, hydrogen bonding interactions might play a less critical role in the biochar-based adsorption of TCH. Notably, over the whole pH range examined, KBCG shows a high level of TCH adsorption, indicating an almost pH-universal adsorption performance driven by the pore filling and π - π stacking interactions.

The impact of the initial TCH concentration on the adsorption capacities is presented in Fig. 5c. For TCH with concentrations below 50 mg/L, the plot of q_e as a function of the initial TCH concentration (C_0) can be well linearly fitted, which can be due to the unoccupied adsorption sites that are sufficient for the low-concentration TCH. With further increasing the TCH concentration, the q_e becomes saturated, and

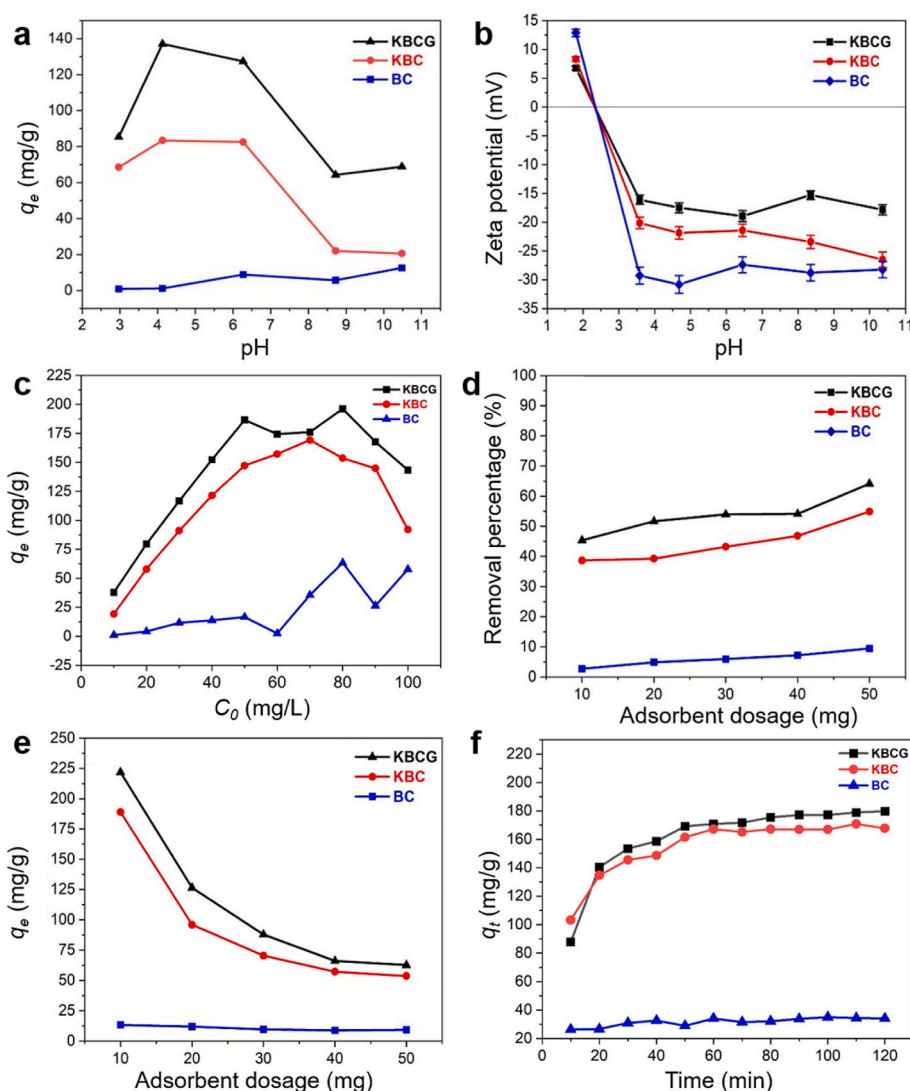


Fig. 5. Impacts of different parameters on the adsorption performances of different biochar-based samples. (a) Impact of the pH on the adsorption capacity. (b) Zeta potential measured under a series of pH conditions. (c) Impact of initial TCH concentration on the adsorption capacity. (d,e) Influence of adsorbent dosages on the TCH removal percentage (d) and equilibrium adsorption capacity (e). (f) Impact of contact time on the adsorption capacity.

an ongoing increase in TCH concentration exerts no positive effects on the adsorption capacity because the number of TCH molecules begins to exceed that of the adsorption sites. When the TCH concentration is raised to 60 mg/L, the solution becomes somewhat viscous due to the aggregation of TCH molecules, which lowers the mass transfer efficiency and therefore is unfavorable for dispersing biochar-based adsorbents [51]. Such observation is more obvious for the case of KBCG, which can be more easily self-aggregated *via* π - π stacking interactions due to the better graphitization achieved by graphene-assisted pyrolysis. Notably, further increasing the TCH concentration beyond 80 mg/L leads to a decrease in q_e , likely due to the more severe aggregation of TCH molecules, as evidenced by the somewhat elevation of the viscosity. This large concentration-induced unfavorable TCH aggregation was also well verified through theoretical studies based on the internal mass transfer resistance model and the Weber and Morris intraparticle diffusion model [51]. The TCH molecule aggregation is prone to block the micropores and mesopores of the KBC and KBCG, thus lowering the q_e . This result reflects the importance of GO-induced biochar pore widening, which can alleviate the negative results from the TCH molecule aggregation.

The result of the adsorbent dosage impact is presented in Fig. 5d and e. An increase in the adsorbent dosage gradually increases the removal percentage due to more adsorption sites that can be provided at higher

dosages (Fig. 5d). On the contrary, the increase of the adsorbent dosage reduces the q_e because the adsorption sites provided by the adsorbent at a lower dosage can be fully used for adsorption, while the higher dosage might result in some adsorption sites free from occupation (Fig. 5e). Moreover, the self-aggregation of the biochar-based adsorbents to a certain extent through π - π stacking interactions also causes some adsorption sites to be buried, where TCH molecules can no longer be accessible. The contact time influence on the amount of TCH captured is shown in Fig. 5f. The hierarchical pores of KBCG enable a faster adsorption process due to the more rapid mass transfer within such widened micropores than the micropores-dominated KBC.

The isothermal adsorption processes of KBCG and KBC at different temperatures are provided in Fig. 6 and Fig. S8 (SD). Around room temperature (303 K), the isothermal adsorption process of KBCG is better fitted by the Langmuir model, thus indicating that the adsorption occurs on the homogenous sites of KBCG in a monolayer manner. The maximum monolayer adsorption capacity (q_m) can be estimated to be 193.43 mg/g (Fig. 6 and Table S3 in the SD), which is superior to many previously reported biochar-based adsorbents in tackling TCH around room temperature (see Table S4 in the SD). Such uniform sites are assumed to be provided by the biochar substrate. The rise of the adsorption temperature from 303 K to 313 K can remarkably increase

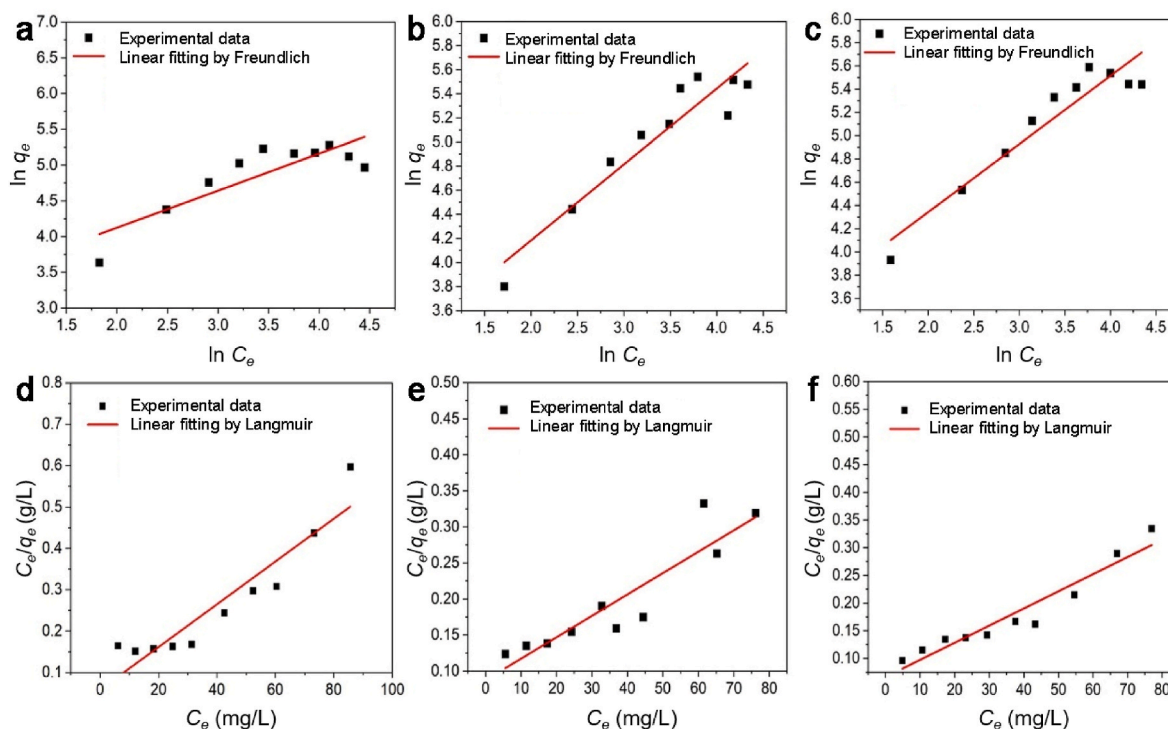


Fig. 6. Isothermal adsorption processes over the KBCG sample. (a–c) Isothermal adsorption processes of KBCG for TCH at 303 K (a), 313 K (b), and 323 K (c) based on the Freundlich model. (d–f) Isothermal adsorption processes of KBCG for TCH at 303 K (d), 313 K (e), and 323 K (f) based on the Langmuir model.

the maximum adsorption amount to 336.70 mg/g, raised by 143.27 mg/g. This increment is significantly larger than 17.29 mg/g achieved by KBC (Fig. S8). The enormous increase in q_m driven by the temperature rise is also accompanied by an increase in the correlation coefficient (R^2) for the Freundlich model-based fitting. These results imply that the

higher temperature can drive the TCH molecules onto the TrGO surface, different adsorption sites from those provided by the biochar matrix, thus making the adsorption sites more heterogeneous (exhibited by the Freundlich model) rather than homogenous (exhibited by the Langmuir model). Such a notable increase in adsorption capacity once the TCH

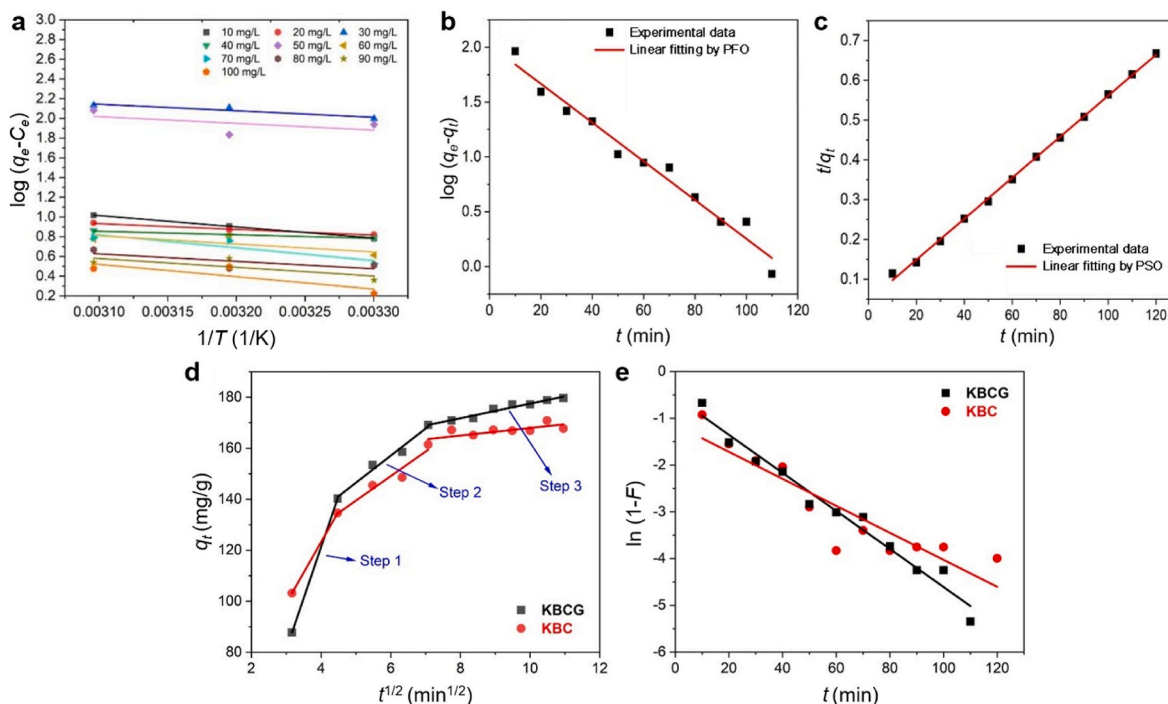


Fig. 7. Analysis of the adsorption thermodynamics, kinetics, and TCH diffusion process. (a) Plot of $\log(q_e/C_e)$ as a function of $1/T$ for a series of adsorption systems with different initial concentrations of TCH using the KBCG adsorbent. (b,c) Fitting of the KBCG-based TCH adsorption process based on the pseudo-first-order (b) and pseudo-second-order (c) kinetic models. (d,e) Fitting the diffusion of TCH molecules onto the KBCG adsorbent based on the intraparticle (d) and liquid-film (e) diffusion models. Note that PFO and PSO represent pseudo-first-order and pseudo-second-order kinetic models, respectively.

molecules interact with the TrGO surface consolidates the excellent adsorption capacity of the graphene composition, which can provide enriched sp^2 -conjugated carbon networks for π - π stacking interactions with the aromatic structure of TCH. The increase in the adsorption capacity at higher temperatures also reveals the endothermic nature of the biochar-based adsorption process. The $1/n$ values calculated based on the Freundlich model are within 0.1–1 for all the cases under different temperatures, indicating the favorable adsorption processes of the biochar-based adsorbents.

The thermodynamic parameters are calculated by Equations 8 and 9 [52]. The results are provided in Fig. 7a, Fig. S9, and Tables S5 and S6 in the SD. The KBCG-based adsorption process is always spontaneous, which is independent of the initial concentration of TCH, as evidenced by the ΔG^θ calculated to be negative in all the cases (Fig. 7a and Table S5 (SD)). By contrast, the KBC-based adsorption process is not always spontaneous since the ΔG^θ is calculated to be positive at a high initial concentration of TCH (i.e., 100 mg/L), as shown in Fig. S9 and Table S6 in the SD. Such a difference between the adsorption processes involving KBCG and KBC can be due to the pore-widening effect of the former compared to the latter. The micropores-to-mesopores transformation driven by the GO additive makes KBCG more adaptable to large-size contaminant molecules such as TCH. As mentioned earlier, TCH molecules aggregate to form large agglomerates at high concentrations (in this case, 100 mg/L), thus requiring larger pore sizes for accommodating agglomerated TCH and promoting mass transfer. Therefore, this result again elucidates the significant role of the GO additive in widening microporous biochar. Besides, the positive values of ΔH^θ and ΔS^θ indicate the endothermal adsorption process and increase of the disorder at the solid-liquid interface after the adsorption, respectively [53].

$$\log \frac{q_e}{C_e} = \frac{\Delta S^\theta}{2.303R} - \frac{\Delta H^\theta}{2.303RT} \quad (8)$$

$$\Delta G^\theta = \Delta H^\theta - T\Delta S^\theta \quad (9)$$

The biochar-based adsorption kinetics are further investigated based on the popular pseudo-first-order and pseudo-second-order kinetic models. The results are provided in Fig. 7b and c, Fig. S10, and Table S7 in the SD. The pseudo-second-order kinetic model is more suitable to describe the kinetic adsorption processes over the biochar-based samples, including BC, KBC, and KBCG, thus revealing that the chemical interactions occur between the adsorbates and the biochar-based adsorbents through electron sharing, transferring, and exchanging. The limited adsorption sites in BC limit the equilibrium adsorption capacity. The KOH-enabled activation notably increases the specific surface area and microporous structure, significantly promoting the adsorption capacity of KBC in stark contrast with BC. Significantly, the GO additive in a small amount can further engineer the micropore structure of the KOH-activated biochar, making the internal structure more accessible and helping expedite the mass transport process in KBCG. As a result, the adsorption kinetics and capacity can be further enhanced relative to KBC.

The intraparticle and liquid-film diffusion models are further adopted to clarify rate-determining steps and mechanisms for the diffusion of the TCH molecules onto the biochar-based adsorbents (Fig. 7d and e, and Table S8 in the SD). Based on these results, we speculate on the following biochar-based adsorption process. First, the liquid-film diffusion dictates the adsorption process to drive the rapid diffusion of TCH molecules onto the exterior surface of KBC and KBCG. Afterward, the adsorption process becomes determined by intraparticle diffusion. Once TCH molecules diffuse into the pore interiors, they are adsorbed onto the internal active sites until saturated. A more detailed discussion can be found in the SD.

Many other adsorption experiments are also considered to evaluate the adsorption performance of KBC and KBCG (see a detailed discussion in the SD), including the anti-interference ability against common metal

ions (Fig. S11), generality in capturing TCH and a range of organic dyes (Figs. S12 and S13), and recyclability and reusability (Fig. S14). The graphene-modified hierarchically porous biochar (i.e., KBCG) is demonstrated to be recyclable, reusable, resistant to interfering metal cations, and universal for binding a range of organic pollutants bearing different charge states, demonstrating equilibrium adsorption capacities of 186.58, 190.38, 268.43, and 254.88 mg/g for TCH, methylene blue, Rhodamine B, and methyl orange, raised by 26.8%, 41.6%, 32.1%, and 105.3%, respectively, compared to the counterpart without GO-enabled micropore widening. The greater adaptability to different-size pollutants presents higher practical application viability.

3.6. Adsorption mechanism analysis

The mechanism underlying the interactions between various biochar-based adsorbents and TCH molecules is further investigated by analyzing the variations of the critical spectra of the KBC and KBCG before and after the adsorption of TCH. Fig. S15 (SD) presents the FTIR absorption spectra of the BC, KBC, and KBCG samples before and after capturing TCH molecules. For the BC sample with a lower graphitization degree and thus fewer π -conjugated carbon networks, its adsorption interactions with TCH molecules enhance the FTIR absorption peak intensity at approximately 1550 cm^{-1} , indexed to the sp^2 -hybridized carbon conjugation structure. BC has a low affinity to TCH molecules due to the fewer π -conjugated carbon networks and hence the weaker π - π stacking interactions. Given that TCH molecules possess an aromatic network, their adsorption onto BC can strengthen the absorption band associated with sp^2 -hybridized carbon. This result also implies that π - π stacking interactions do not occur effectively between BC and TCH; otherwise, the absorption band intensity is depressed. Indeed, for KBC bearing a better graphitization and hence more sp^2 -hybridized carbon networks, the π - π stacking interactions between KBC and TCH inhibit the FTIR absorption peak related to sp^2 -conjugated carbon. More notably, KBCG presents a somewhat weakened peak ascribed to the sp^2 -conjugated carbon network, revealing that KBCG can impart stronger π - π stacking interactions compared with KBC due to the incorporation of TrGO with a high fraction of sp^2 -conjugated structure. Except for such a characteristic peak, other absorption bands almost overlap for the biochar-based samples before and after absorbing TCH, implying the weak hydrogen bonding interactions between the functional groups of the biochar-based adsorbents and TCH molecules.

Raman spectra of the biochar-based adsorbents before and after the adsorption of TCH can also verify the GO additive-imparted micropore widening (Fig. S16 in the SD). The BC sample with poor porosity and low specific surface area exhibit almost overlapped Raman spectra before and after binding with TCH molecules, which indicates that the limited number of TCH molecules on BC surface bearing few active sites cannot significantly change the Raman spectra of BC (Fig. S16a). A notable difference in Raman spectra can be found between the KBC sample before and after tethering TCH (Fig. S16b). This is because KBC possesses a large specific surface area and microporous structure. The small size of the micropores of KBC blocks the diffusion of TCH molecules into the internal micropores, implying that many TCH molecules are attached to the external surface of KBC (Fig. S17 in the SD). While Raman spectroscopy is a surface-sensitive tool for material characterizations, the high quantity of TCH molecules on the external surface of KBC significantly changes the Raman spectrum. On the other hand, the widened porous structure of KBCG relative to KBC makes part of TCH molecules diffuse into the internal of the porous structure (Fig. S17), which signifies that the TCH molecules can be more homogeneously dispersed all over the KBCG body, both external and interior. Thus, the Raman spectra of KBCG are less influenced when compared with that of the KBC system (Fig. S16c). The results obtained via Raman spectroscopy again support our early statement that the GO-driven micropore widening is essential for further enhancing the adsorption performance of activated biochar.

XPS spectra are further provided in Fig. 8a–f to disclose the adsorption interactions between typical biochar-based adsorbents (*i.e.*, KBC and KBCG) and TCH molecules. The high-resolution XPS C1s and O1s spectra of KBC before and after tethering TCH are presented in Fig. 8a and b, respectively. The KBC bound with TCH exhibits an enhanced shoulder deconvoluted at approximately 287 eV compared with the pristine KBC counterpart (Fig. 8a). This shoulder strengthening mainly originates from the TCH molecules attached to KBC. A significant shift cannot be found for the deconvoluted XPS peak associated with the C–O/C–N groups after TCH capturing in both XPS C1s and O1s spectra (Fig. 8a and b), revealing hydrogen bonds between KBC and TCH are not significant. Likewise, the deconvoluted peak at about 288 eV, corresponding to C=O groups, is strengthened and without a notable shift, thus indicating that C=O groups of KBC are also not involved in the adsorption interactions with TCH. The adsorption of TCH onto KBC lowers the intensity of the deconvoluted peak around 290 eV with an evident shift (particularly in the XPS O1s spectrum, Fig. 8b), revealing that the COOH groups of KBCG participate in the adsorption interactions with TCH *via* electrostatic interactions. Impressively, the satellite peak at a high binding energy, stemming from π - π^* transition, disappears completely after adsorbing TCH onto the KBC matrix (Fig. 8a), thus implying that the π - π interactions play a critical role in the biochar-based adsorption of TCH. The high-resolution XPS N1s spectra of KBC in Fig. 8c disclose that almost all these N configurations participate in TC adsorption, especially pyridinic and pyrrolic N based on hydrogen bonding interactions, as evidenced by more conspicuous shifts. Considering the trace N groups in KBC (Table S1 in the SD), the hydrogen-bonding interactions between pyridinic N and TCH are limited.

For the KBCG samples before and after tethering TCH, they exhibit similar XPS C1s spectra to those for KBC (*e.g.*, the disappearance of satellite peak at high binding energy due to π - π^* transition), revealing

that π - π stacking interactions are pivotal in the KBCG-based adsorption interactions (Fig. 8d). Notably, the difference in the high-resolution XPS O1s spectra of the KBCG samples before and after capturing TCH is more significant than that of the KBC counterparts, which might imply that TCH molecules can interact with the O/N-containing functional groups in the internal porous structure of KBCG rather than solely on the exterior surface as KBC does. This finding again verifies a significant GO-driven-biochar micropore widening effect on the adsorption performance improvement (Fig. 8e and f).

4. Conclusion

The GO additive-induced partial transformation of KOH-activated biochar micropores into mesopores was achieved to enhance the pollutant-capturing ability. The micropore widening of the microporous biochar (with the average pore size increased from 3.0 to 3.3 nm) brought several benefits. First, mass transport was improved, as revealed by adsorption kinetic studies. Second, the accessibility to pore interiors is enhanced, as evidenced by *ex-situ* Raman and XPS spectroscopies and N₂ physisorption tests. Third, the compatibility with large-size contaminant molecules was raised, as verified by the adsorption behavior comparison between KBCG and KBC. Meanwhile, the graphene-assisted pyrolysis could impart a larger fraction of the sp²-hybridized carbon network for the biochar matrix, with the sp²-to-sp³ carbon ratio increased from 0.59 to 0.79, thus facilitating π - π stacking interactions between KBCG and TCH. Consequently, TCH adsorption over KBCG was significantly strengthened (including adsorption capacity and kinetics), with the *q_m* estimated as 193.43 and 336.70 mg/g at 303 and 313 K, respectively. Thorough adsorption mechanism analysis, including adsorption isotherms, kinetics, and thermodynamics, impacts of various parameters on the adsorption behaviors, and comparisons of the biochar-based adsorbents before and after capturing

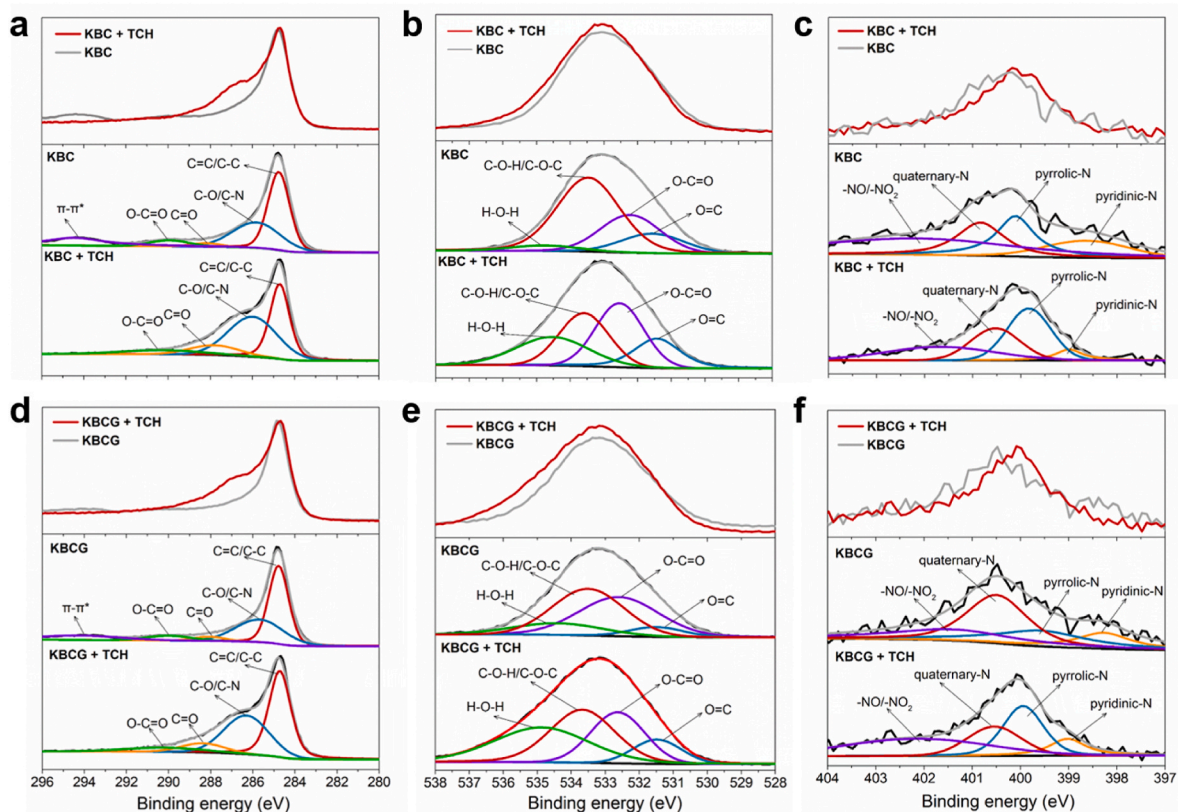


Fig. 8. Biochar-based adsorption mechanism analysis based on XPS spectrum variation with TCH adsorption. (a–f) High-resolution XPS C1s (a and d), O1s (b and e), and N1s (c and f) spectra of KBC (a–c) and KBCG (d–f) before and after adsorbing TCH molecules.

TCH, we confirmed that π - π stacking interactions played a critical role in binding TCH and other aromatic organic dyes. In contrast, electrostatic attraction and hydrogen bonding interactions were less involved in TC adsorption. The micropore widening also rendered the pore filling vital in the homogenous adsorption of TCH all over the hierarchically porous KBCG body, in contrast to the microporous KBC, where TCH was primarily adsorbed on the exterior surface. Furthermore, apart from superior adsorption capacity, KBCG was also demonstrated to be recyclable, reusable, resistant to the typical interfering metal cations commonly existing in tap water, and universal for a range of organic contaminants bearing different charge states. Significantly, the GO-enabled biochar micropore widening rendered 26.8%, 41.6%, 32.1%, and 105.3% increases in q_e for the uptake of TCH, MB, RhB, and MO, respectively, compared to the counterpart without GO-imparted micropore widening. This work opens up a reliable, universal, low-cost, and straightforward avenue to engineering the porous structure of biochar materials, which will be highly significant for many critical applications beyond environmental remediation.

CRediT authorship contribution statement

Yaoheng Liang: Conceptualization, Writing – original draft, and, Writing – review & editing. **Xuejun Xu:** Conceptualization, Writing – original draft, and, Writing – review & editing. **Fangzheng Yuan:** Conceptualization, Writing – original draft, and, Writing – review & editing. **Yinlei Lin:** Methodology, Resources, and, Writing – review & editing. **Yisheng Xu:** Methodology, Resources, and, Writing – review & editing. **Yuyuan Zhang:** Methodology, Resources, and, Writing – review & editing. **Dongchu Chen:** Resources, Writing – review & editing. **Wenyi Wang:** Resources, Writing – review & editing. **Huawen Hu:** Conceptualization, Funding acquisition, Formal analysis, Project administration, and, Writing – review & editing. **Jian Zhen Ou:** Conceptualization, Funding acquisition, Formal analysis, Project administration, and, Writing – review & editing.

Declaration of competing interest

The authors declare that they have no known competing financial interests or personal relationships that could have appeared to influence the work reported in this paper.

Acknowledgements

This work was financially supported by the Guangdong Provincial Education Department Special Project of Key Research Areas (2020ZDZX2066), the Key Project of Guangdong Basic and Applied Basic Research Foundation (2020B1515120081), and the National Natural Science Foundation of China (51702050, 51906045).

Appendix A. Supplementary data

Supplementary data to this article can be found online at <https://doi.org/10.1016/j.carbon.2023.01.023>.

References

- [1] J. Qian, X. Gao, B. Pan, Nanoconfinement-mediated water treatment: from fundamental to application, *Environ. Sci. Technol.* 54 (14) (2020) 8509–8526.
- [2] S. Choi, W. Sim, D. Jang, Y. Yoon, J. Ryu, J. Oh, J.-S. Woo, Y.M. Kim, Y. Lee, Antibiotics in coastal aquaculture waters: occurrence and elimination efficiency in oxidative water treatment processes, *J. Hazard Mater.* 396 (2020), 122585.
- [3] Y. Hu, X. Wei, Q. Zhu, L. Li, C. Liao, G. Jiang, COVID-19 pandemic impacts on humans taking antibiotics in China, *Environ. Sci. Technol.* 56 (12) (2022) 8338–8349.
- [4] C.A. Morales-Paredes, J.M. Rodríguez-Díaz, N. Boluda-Botella, Pharmaceutical compounds used in the COVID-19 pandemic: a review of their presence in water and treatment techniques for their elimination, *Sci. Total Environ.* 814 (2022), 152691.
- [5] X. Xu, Y. Xu, Y. Liang, H. Long, D. Chen, H. Hu, J.Z. Ou, Vacancies-modified g-C₃N₄ and their photocatalytic applications, *Mater. Chem. Front.* 6 (2022) 3143–3173.
- [6] X. Shi, A. Tian, J. You, H. Yang, Y. Wang, X. Xue, Degradation of organic dyes by a new heterogeneous Fenton reagent - Fe₂GeS₄ nanoparticle, *J. Hazard Mater.* 353 (2018) 182–189.
- [7] H. Hu, J.H. Xin, H. Hu, X. Wang, D. Miao, Y. Liu, Synthesis and stabilization of metal nanocatalysts for reduction reactions – a review, *J. Mater. Chem.* 3 (21) (2015) 11157–11182.
- [8] M. Bilal, M. Adeel, T. Rasheed, Y. Zhao, H.M.N. Iqbal, Emerging contaminants of high concern and their enzyme-assisted biodegradation – a review, *Environ. Int.* 124 (2019) 336–353.
- [9] W. Wang, J. Chiou, W. Chen, C. Kan, T.Y.C. Lam, H. Hu, Poly(hexamethylene biguanide): an efficient pH-tolerant and salt-intensive flocculant in the removal of anionic dyes from wastewater, *J. Mater. Sci.* 57 (32) (2022) 15662–15673.
- [10] H. Hu, H. Quan, B. Zhong, Z. Li, Y. Huang, X. Wang, M. Zhang, D. Chen, A reduced graphene oxide quantum dot-based adsorbent for efficiently binding with organic pollutants, *ACS Appl. Nano Mater.* 1 (11) (2018) 6502–6513.
- [11] M. Yu, J. Wang, L. Tang, C. Feng, H. Liu, H. Zhang, B. Peng, Z. Chen, Q. Xie, Intimate coupling of photocatalysis and biodegradation for wastewater treatment: mechanisms, recent advances and environmental applications, *Water Res.* 175 (2020), 115673.
- [12] H. Hu, M. Chang, M. Zhang, X. Wang, D. Chen, A new insight into PAM/graphene-based adsorption of water-soluble aromatic pollutants, *J. Mater. Sci.* 52 (14) (2017) 8650–8664.
- [13] H. Hu, W. Wen, J.Z. Ou, Construction of adsorbents with graphene and its derivatives for wastewater treatment: a review, *Environ. Sci.-Nano* 9 (9) (2022) 3226–3276.
- [14] Y. Xu, Y. Liang, Q. He, R. Xu, D. Chen, X. Xu, H. Hu, Review of doping SrTiO₃ for photocatalytic applications, *Bull. Mater. Sci.* 46 (2023) 6.
- [15] J. Wang, S. Wang, Preparation, modification and environmental application of biochar: a review, *J. Clean. Prod.* 227 (2019) 1002–1022.
- [16] P. Sharma, A.K. Singh, V.K. Shahi, Selective adsorption of Pb(II) from aqueous medium by cross-linked chitosan-functionalized graphene oxide adsorbent, *ACS Sustainable Chem. Eng.* 7 (1) (2018) 1427–1436.
- [17] K. Gupta, O.P. Khatri, Reduced graphene oxide as an effective adsorbent for removal of malachite green dye: plausible adsorption pathways, *J. Colloid Interface Sci.* 501 (2017) 11–21.
- [18] H. Hu, W. Liang, Y. Zhang, S. Wu, Q. Yang, Y. Wang, M. Zhang, Q. Liu, Multipurpose use of a corn cob biomass for the production of polysaccharides and the fabrication of a biosorbent, *ACS Sustainable Chem. Eng.* 6 (3) (2018) 3830–3839.
- [19] D. Ying, P. Hong, F. Jiali, T. Qinqin, L. Yuhui, W. Youqun, Z. Zhibin, C. Xiaohong, L. Yunhai, Removal of uranium using MnO₂/orange peel biochar composite prepared by activation and *in-situ* deposit in a single step, *Biomass Bioenergy* 142 (2020), 105772.
- [20] Y. Zhang, J. Zhang, K. Chen, S. Shen, H. Hu, M. Chang, D. Chen, Y. Wu, H. Yuan, Y. Wang, Engineering banana-peel-derived biochar for the rapid adsorption of tetracycline based on double chemical activation, *Resour. Conserv. Recycl.* 190 (2023), 106821.
- [21] Y. Zhang, L. Deng, H. Hu, Y. Qiao, H. Yuan, D. Chen, M. Chang, H. Wei, Pomelo peel-derived, N-doped biochar microspheres as an efficient and durable metal-free ORR catalyst in microbial fuel cells, *Sustain. Energy Fuels* 4 (4) (2020) 1642–1653.
- [22] L. Bai, X. Xu, J. Feng, S. Ma, Preparation of sugarcane bagasse biochar/nano-iron oxide composite and mechanism of its Cr (VI) adsorption in water, *J. Clean. Prod.* 320 (2021), 128723.
- [23] J. Zhang, Y. Zhang, H. Huang, K. Huang, L. Deng, H. Hu, M. Chang, D. Chen, Y. Wang, Exploration of highly porous biochar derived from dead leaves to immobilize LiOH-H₂O nanoparticles for efficient thermochemical heat storage applications, *Energy Technol.* 10 (5) (2022), 2101127.
- [24] L. Deng, H. Yuan, X. Qian, Q. Lu, L. Wang, H. Hu, Y. Chen, Municipal sludge-derived carbon dots-decorated, N-doped hierarchical biocarbon for the electrochemical reduction of carbon dioxide, *Resour. Conserv. Recycl.* 177 (2022), 105980.
- [25] P. Krasucka, B. Pan, Y. Sik Ok, D. Mohan, B. Sarkar, P. Oleszczuk, Engineered biochar – a sustainable solution for the removal of antibiotics from water, *Chem. Eng. J.* 405 (2021), 126926.
- [26] H. Hu, J.H. Xin, H. Hu, X. Wang, Y. Kong, Metal-free graphene-based catalyst—insight into the catalytic activity: a short review, *Appl. Catal. Gen.* 492 (2015) 1–9.
- [27] X. Wang, Y. Zhang, R. Shan, H. Hu, Polydopamine interface encapsulating graphene and immobilizing ultra-small, active Fe₃O₄ nanoparticles for organic dye adsorption, *Ceram. Int.* 47 (3) (2021) 3219–3231.
- [28] H. Hu, C.C.K. Allan, J. Li, Y. Kong, X. Wang, J.H. Xin, H. Hu, Multifunctional organically modified graphene with super-hydrophobicity, *Nano Res.* 7 (3) (2014) 418–433.
- [29] L. Leng, Q. Xiong, L. Yang, H. Li, Y. Zhou, W. Zhang, S. Jiang, H. Li, H. Huang, An overview on engineering the surface area and porosity of biochar, *Sci. Total Environ.* 763 (2021), 144204.
- [30] C. Li, X. Zhu, H. He, Y. Fang, H. Dong, J. Lü, J. Li, Y. Li, Adsorption of two antibiotics on biochar prepared in air-containing atmosphere: influence of biochar porosity and molecular size of antibiotics, *J. Mol. Liq.* 274 (2019) 353–361.
- [31] H. Liu, G. Xu, G. Li, Preparation of porous biochar based on pharmaceutical sludge activated by NaOH and its application in the adsorption of tetracycline, *J. Colloid Interface Sci.* 587 (2021) 271–278.

- [32] J. Xu, Y. Zhang, B. Li, S. Fan, H. Xu, D.X. Guan, Improved adsorption properties of tetracycline on KOH/KMnO₄ modified biochar derived from wheat straw, *Chemosphere* 296 (2022), 133981.
- [33] M. Hosny, M. Fawzy, A.S. Eltaweil, Green synthesis of bimetallic Ag/ZnO@Biochar nanocomposite for photocatalytic degradation of tetracycline, antibacterial and antioxidant activities, *Sci. Rep.* 12 (1) (2022) 7316.
- [34] H. Chen, X. Wang, J. Li, X. Wang, Cotton derived carbonaceous aerogels for the efficient removal of organic pollutants and heavy metal ions, *J. Mater. Chem.* 3 (11) (2015) 6073–6081.
- [35] Y. Ma, L. Wu, P. Li, L. Yang, L. He, S. Chen, Y. Yang, F. Gao, X. Qi, Z. Zhang, A novel, efficient and sustainable magnetic sludge biochar modified by graphene oxide for environmental concentration imidacloprid removal, *J. Hazard Mater.* 407 (2021), 124777.
- [36] H. Hu, J.H. Xin, H. Hu, X. Wang, Structural and mechanistic understanding of an active and durable graphene carbocatalyst for reduction of 4-nitrophenol at room temperature, *Nano Res.* 8 (12) (2015) 3992–4006.
- [37] J. Liu, Z. Huang, Z. Chen, J. Sun, Y. Gao, E. Wu, Resource utilization of swine sludge to prepare modified biochar adsorbent for the efficient removal of Pb(II) from water, *J. Clean. Prod.* 257 (2020), 120322.
- [38] W. Ahmed, S. Mehmood, A. Núñez-Delgado, S. Ali, M. Qaswar, Z.H. Khan, H. Ying, D.-Y. Chen, Utilization of Citrullus lanatus L. seeds to synthesize a novel MnFe₂O₄-biochar adsorbent for the removal of U(VI) from wastewater: insights and comparison between modified and raw biochar, *Sci. Total Environ.* 771 (2021), 144955.
- [39] J.S.d.S. Carneiro, D.A.d.C. Leite, G.M.d. Castro, J.R. Franca, L. Botelho, J.R. Soares, J.E.d. Oliveira, L.C.A. Melo, Biochar-graphene oxide composite is efficient to adsorb and deliver copper and zinc in tropical soil, *J. Clean. Prod.* 360 (2022), 132170.
- [40] S. Xiong, Z. Wu, Z. Li, Facile fabrication of robust, versatile, and recyclable biochar-graphene oxide composite monoliths for efficient removal of different contaminants in water, *Chemosphere* 287 (2022), 132418.
- [41] Y. Gao, Z. Fang, W. Lin, H. Chen, A. Bhatnagar, J. Li, Y. Xie, Y. Bao, J. Chen, H. Zhao, J. Meng, W. Chen, H. Wang, Large-flake graphene-modified biochar for the removal of bisphenol S from water: rapid oxygen escape mechanism for synthesis and improved adsorption performance, *Environ. Pollut.* 317 (2023), 120847.
- [42] Y. Luo, P. Yin, G. Wu, L. Zhang, G. Ma, J. Wang, X. Sun, G. Bu, Porous carbon sphere decorated with Co/Ni nanoparticles for strong and broadband electromagnetic dissipation, *Carbon* 197 (2022) 389–399.
- [43] H. Hu, X. Wang, D. Miao, Y. Wang, C. Lai, Y. Guo, W. Wang, J.H. Xin, H. Hu, A pH-mediated enhancement of the graphene carbocatalyst activity for the reduction of 4-nitrophenol, *Chem. Commun.* 51 (93) (2015) 16699–16702.
- [44] A.A. Balandin, S. Ghosh, W. Bao, I. Calizo, D. Teweldebrhan, F. Miao, C.N. Lau, Superior thermal conductivity of single-layer graphene, *Nano Lett.* 8 (3) (2008) 902–907.
- [45] F.G.d.A. Dias, A.G. Veiga, A.P.A.d.C.P. Gomes, M.F. da Costa, M.L.M. Rocco, Using XPS and FTIR spectroscopies to investigate polyamide 11 degradation on aging flexible risers, *Polym. Degrad. Stabil.* 195 (2022), 109787.
- [46] X. Guan, G. Chen, C. Shang, ATR-FTIR and XPS study on the structure of complexes formed upon the adsorption of simple organic acids on aluminum hydroxide, *J. Environ. Sci.* 19 (4) (2007) 438–443.
- [47] R. Arrigo, M. Hävecker, M.E. Schuster, C. Ranjan, E. Stotz, A. Knop-Gericke, R. Schlögl, *In situ* study of the gas-phase electrolysis of water on platinum by NAP-XPS, *Angew. Chem. Int. Ed.* 52 (44) (2013) 11660–11664.
- [48] F. Abbaci, A. Nait-Merzoug, O. Guellati, A. Harat, J. El Haskouri, J. Delhalle, Z. Mekhalif, M. Guerioune, Bio/KOH ratio effect on activated biochar and their dye based wastewater depollution, *J. Anal. Appl. Pyrolysis* 162 (2022), 105452.
- [49] H. Peng, Y. Li, J. Wen, X. Zheng, Synthesis of ZnFe₂O₄/B,N-codoped biochar via microwave-assisted pyrolysis for enhancing adsorption-photocatalytic elimination of tetracycline hydrochloride, *Ind. Crop. Prod.* 172 (2021), 114066.
- [50] Y. Qin, B. Chai, C. Wang, J. Yan, G. Fan, G. Song, Removal of tetracycline onto KOH-activated biochar derived from rape straw: affecting factors, mechanisms and reusability inspection, *Colloids Surf., A* 640 (2022), 128466.
- [51] A.N. Módenes, G. Bazarin, C.E. Borba, P.P.P. Locatelli, F.P. Borsato, V. Pagno, R. Pedrini, D.E.G. Trigueros, F.R. Espinoza-Quinones, F.B. Scheufele, Tetracycline adsorption by tilapia fish bone-based biochar: mass transfer assessment and fixed-bed data prediction by hybrid statistical-phenomenological modeling, *J. Clean. Prod.* 279 (2021), 123775.
- [52] C. Yang, Y. Zhu, J. Wang, W. Sun, L. Yang, H. Lin, S. Lv, A novel granular MOF composite with dense and ordered MIL-100(Fe) nanoparticles grown on porous alumina: green synthesis and enhanced adsorption of tetracycline hydrochloride, *Chem. Eng. J.* 426 (2021), 131724.
- [53] B.K. Chandra, A. Majee, A. Bhaumik, A cationic porous polymer as a robust and recyclable adsorbent for the removal of harmful dyes from aqueous contaminants, *Environ. Sci.-Nano* 9 (2022) 3943–3956.